

---

# Self-Generated Magnetic Fields in Direct-Drive–Implosion Experiments

## Introduction

Self-generated magnetic fields in laser-produced plasma are developed by the rate  $\partial \mathbf{B} / \partial t \sim \nabla T_e \times \nabla n_e$  (Ref. 1), where  $\mathbf{B}$  is the magnetic induction and  $n_e$  and  $T_e$  denote the electron number density and temperature, respectively. Such fields were first observed in experiments using high-power laser beams focused into a gas<sup>2</sup> and onto a solid target.<sup>3–5</sup> In perfectly spherical direct-drive implosions,<sup>6</sup>  $\nabla T_e \times \nabla n_e = 0$ ; therefore, they cannot develop self-generated fields. Fields are expected in real implosions where various perturbations are present, resulting in noncollinear  $\nabla T_e$  and  $\nabla n_e$ . Such perturbations may be seeded by nonuniform laser irradiation (e.g., laser imprint), target defects (e.g., surface roughness and surface contaminations), target mounts, and other sources. The strong dependency on temperature makes the field-generation process most efficient in the hottest regions of implosion targets, such as the ablated corona during the laser drive and the target center at the moment of maximum compression. Self-generated magnetic fields cannot approach high, dynamically important values in laser-produced plasma because of the relatively low efficiency source (the energy density of the fields can be only a fraction of the thermal energy density) and typically significant resistive dissipations. Estimates show that the maximum energy density of the fields does not exceed a few percent of the plasma's thermal energy density (i.e., plasma  $\beta \gtrsim 100$ ). Nevertheless, self-generated magnetic fields can alter implosions by suppressing and redirecting heat fluxes.<sup>7</sup>

Heat transport provided by electrons<sup>8</sup> is an important mechanism in direct-drive implosions that delivers the laser energy deposited near the critical radius  $R_{cr}$ , in which  $n_e = n_{cr}$ , to the ablation front through a conduction zone.<sup>6</sup> Here  $n_{cr}$  is the critical density when the laser frequency equals the plasma frequency. Self-generated magnetic fields in the conduction zone can affect heat fluxes and, therefore, affect target drive, symmetry, and implosion performance. Magnetic fields can considerably change the transport coefficients, such as the electron and thermal conductivity, when the Hall parameter  $\omega_e \tau_e \gtrsim 0.3$  (Ref. 9), where  $\omega_e = eB/m_e c$ ;  $c$  is the speed of light,  $m_e$  and

$e$  are the electron mass and charge, respectively, and  $\tau_e$  is the electron–ion collision time. Simulations predict that magnetic fields in direct-drive–implosion experiments on the OMEGA laser<sup>10</sup> can grow up to several MG and the Hall parameter can approach  $\sim 0.3$  near the ablation surface. This makes the field effects important in the conditions relevant to inertial confinement fusion (ICF) and requires experimental validation.

Magnetic fields in laser-produced plasma have been measured using coils,<sup>2</sup> Faraday rotation of optical probe beams,<sup>5</sup> polarimetry measurements of self-generated laser harmonics,<sup>11</sup> and proton radiography.<sup>12,13</sup> The latter method infers electromagnetic fields by measuring deflection and energy loss of protons while traversing the plasma. Two techniques are typically employed to generate probe protons. In the first technique, a glass microballoon with  $D^3He$  fuel is imploded to produce 14.7- and 3-MeV fusion monoenergetic protons.<sup>13</sup> In the second technique, broad energy spectrum protons with an energy from zero up to several tens of MeV are generated via the target's normal sheath acceleration (TNSA) mechanism, where strong sheath electric fields are produced using a high-intensity ( $\sim 10^{19}$  W/cm<sup>2</sup>) laser interaction with a solid target.<sup>14</sup> Divergent proton flows generated by the TNSA technique have a small virtual source size (about several microns) and good laminarity, providing better spatial and temporal resolutions than those provided by the fusion-based technique.<sup>15</sup>

Protons in the range of  $\sim 10$  to 60 MeV are suitable for probing  $\sim$ MG magnetic fields and electric fields of  $\sim 10^7$  V/cm in experiments with laser-produced plasmas.<sup>16–18</sup> Experiments on OMEGA using the fusion-based proton backlighter and plastic planar foils driven at an intensity of  $10^{14}$  to  $10^{15}$  W/cm<sup>2</sup> indicate the development of millimeter-scale magnetic loops<sup>19</sup> localized at the edge of the laser spot, which have been predicted theoretically.<sup>20</sup> Rayleigh–Taylor-induced magnetic fields up to about 1 MG have been measured in accelerated foils during the linear growth for 120- $\mu$ m-wavelength perturbations.<sup>21</sup> Planar-foil experiments on OMEGA using TNSA proton backlighters demonstrated about 10- $\mu$ m resolution of electromagnetic field

structures. This resolution allows one to investigate small-scale magnetic fields associated with Rayleigh–Taylor spikes and bubbles in laser-accelerated foils.<sup>22,23</sup>

The first application of proton radiography to direct-drive implosions was demonstrated on the six-beam Vulcan laser.<sup>24</sup> Direct-drive-implosion experiments on OMEGA using fusion-based proton backlighters found a complex evolution of electromagnetic structures.<sup>25</sup> Imploding capsules develop radial electric fields of  $\sim 10^7$  V/cm, reversing directions during the implosion following the evolution of the electron pressure gradient.<sup>26</sup> More-recent OMEGA direct-drive-implosion experiments employing TNSA proton backlighters found that proton images at late implosion times (after the end of the laser pulse) are dominated by random filamentary structures formed by small-scale electromagnetic fields in the outer corona.<sup>15</sup> These fields screen the regular fields near the target surface and limit the applicability of the TNSA proton radiography.

This work focuses on measurements and simulations of electromagnetic fields in direct-drive OMEGA implosions during an early implosion time, when the screening effect of the fields in the corona is small. Various surface defects (wires, glue spots, and mount stalks) were imposed to enhance self-generated magnetic fields, which were measured by the TNSA proton backlighter technique. Measured proton radiographs were compared with synthetic radiographs produced using the two-dimensional (2-D) magnetohydrodynamic (MHD) ICF code *DRACO*<sup>27</sup> and a proton ray-trace code. The MHD model in *DRACO* is based on the Braginskii model<sup>1</sup> and includes the field source, Nernst convection,<sup>28,29</sup> anisotropic resistivity, and field-modified heat fluxes.

This article describes the experimental setup and measurements; compares the measurements with *DRACO* simulations; and concludes with a discussion of the results of the experiment and simulations. Details of the MHD model in *DRACO* are presented in the Appendix.

## Experiments

Figure 138.10 shows a schematic of the direct-drive-implosion experiment employing the TNSA proton radiography. A 860- $\mu\text{m}$ -diam plastic-shell target was imploded using 60 OMEGA laser beams with a 1-ns square pulse delivering about 28 kJ on target. This corresponds to an on-target intensity of  $I \approx 1.2 \times 10^{15}$  W/cm<sup>2</sup>. Standard OMEGA SG4 distributed phase plates,<sup>30</sup> polarization smoothing,<sup>31</sup> and smoothing by spectral dispersion<sup>32</sup> were employed to uniformly illuminate the target. The implosion was backlit at a specified time with a proton beam, which was generated by the interaction of a 10-ps, high-intensity ( $I \sim 2 \times 10^{19}$  W/cm<sup>2</sup>) OMEGA EP<sup>33</sup> beam with a 10- $\mu\text{m}$ -thick Au foil. The protons had an energy range of 0 to  $\sim 60$  MeV with an almost exponential distribution. They formed images on radiochromic films, which were arranged in packs that consisted of interleaved filters (Al or Ta) and films. Each film was sensitive to protons from a specific energy interval. More details of the employed radiography technique can be found in Ref. 15.

Four 27- $\mu\text{m}$ -thick plastic-shell (CH) targets having different imposed surface defects were imploded. These targets were supported by mount stalks, each of which was an  $\sim 80$ - $\mu\text{m}$ -diam carbon–silicon fiber glued normally to the target surface (see Fig. 138.11). The glue at the stalk and target joint formed a 120- to 160- $\mu\text{m}$ -diam circular spot on the target surface. These

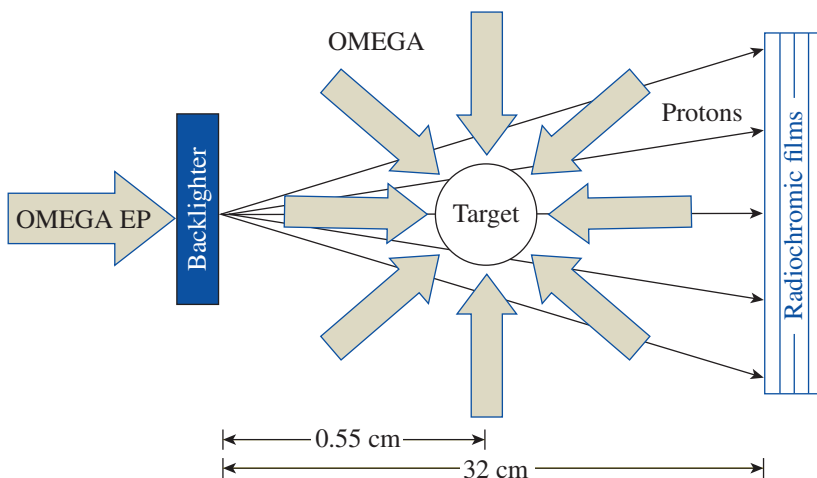


Figure 138.10

Schematic of the experiment. A plastic-shell target was imploded using 60 OMEGA laser beams and backlit by protons having an energy range of 0 to  $\sim 60$  MeV. The protons were generated using a high-intensity OMEGA EP laser beam. Images from different energy protons were obtained using a radiochromic film pack.

glue spots and stalks introduced perturbations that were the source of electromagnetic fields. A piece of 20- $\mu\text{m}$ -diam Cu wire was glued to the surface of three of the targets. Each wire encircled the target, covering half of the equator. These wires were located on the targets' hemispheres, which faced either the proton backlighter (source) or film pack (detector). One target had a 50- $\mu\text{m}$ -diam glue spot located on the hemisphere, facing the detector. Figures 138.11(a) and 138.11(b) show pre-shot images of the targets with the wire and glue spot, respectively. The stalk mount forms a  $42^\circ$  angle with the imaging axis.

Figure 138.12 shows proton radiographs of the implosion targets from film #9 of the packs. These films are primarily sensitive to 36.8-MeV protons.<sup>15</sup> The target center is projected in the center of the radiographs. The evolution times in Figs. 138.12(a)–138.12(d) are  $t = 300, 525, 770,$  and  $770$  ps, respectively, where  $t = 0$  corresponds to the beginning of the laser pulse. This timing was estimated by accounting for the proton time-of-flight delays and has an uncertainty of  $\Delta t \approx 5$  ps.

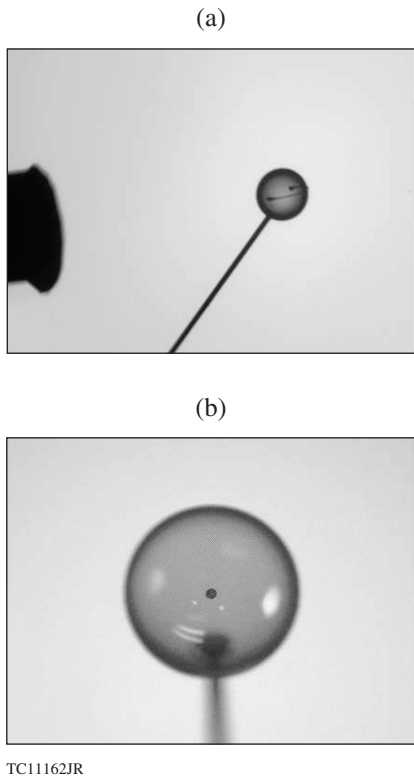


Figure 138.11  
Pre-shot images of implosion targets. (a) An 860- $\mu\text{m}$ -diam plastic-shell target on a stalk mount. The stalk axis forms a  $42^\circ$  angle with the imaging axis. A piece of Cu wire, 20  $\mu\text{m}$  in diameter and half the target diameter in length, was glued to the target surface. The dark image on the left is a proton backlighter assembly. (b) Target with a 50- $\mu\text{m}$ -diam glue spot viewed from the proton-detector side.

The targets with the wire on the side facing the detector are shown in Figs. 138.12(a) and 138.12(c), and the target with the wire facing the source is shown in Fig. 138.12(d). The target with the glue spot located on the side facing the detector is shown in Fig. 138.12(b).

The radiographs in Fig. 138.12 reveal multiple ring structures around the targets. Similar structures were reported in previous studies using the fusion-based backlighters.<sup>25</sup> The outer dark ring A appears only in Fig. 138.12(a) at the early implosion time  $t = 300$  ps, while the white rings B are observed in the early and late time radiographs in Fig. 138.12. The radius of ring B is reduced with time, apparently following the reduction of the radius of the implosion targets. Simulations suggest (see **Simulation Results**, p. 114) that electric fields cause the observed ring structures to form. In particular, ring A is formed because of the fields localized at the front of the expanding corona. This front quickly moves, leaving the field of view of the proton diagnostics; therefore, the ring is not observed at the

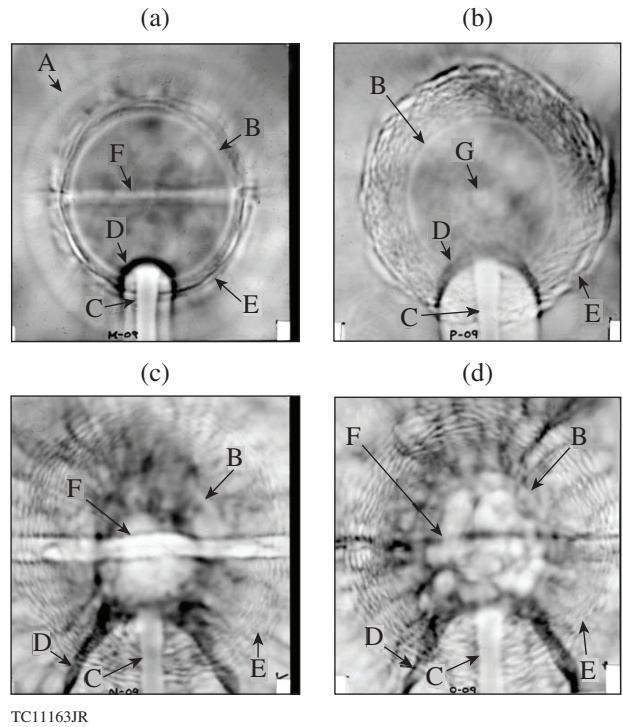


Figure 138.12  
Radiographs of implosion targets from film #9 (primarily sensitive to 37-MeV protons). Darker regions correspond to higher fluence. (a) Target with a Cu wire on the side facing the proton detector at  $t = 300$  ps (shot 63035). (b) Target with a glue spot on the side facing the proton detector at  $t = 525$  ps (shot 63043). [(c) and (d)] Targets with Cu wires on the sides facing the proton detector and source, respectively, at  $t = 770$  ps (shots 63037 and 63039, respectively).

later times. Rings B are associated with the critical radius  $R_{cr}$ , where  $n_e$  and  $T_e$  experience significant variations, resulting in large electric fields.

The radiographs in Fig. 138.12 also reveal quasi-spherically distributed ripple structures E observed outside of rings B. These structures consist of many dark and light filaments elongated in the azimuthal direction. The ripple structure in Fig. 138.12(a) is located inside ring A and occupies a relatively narrow radial range. At a later time, in Fig. 138.12(b), this structure increases the radial range and develops a sharp outer edge at  $\sim 800 \mu\text{m}$  from target center. At an even later time, in Figs. 138.12(c) and 138.12(d), the structure E is still seen to occupy about the same radial range as in Fig. 138.12(b) but is missing the sharp outer edge.

The white rings B in the radiographs from the same film pack show different diameters, depending on the proton energy. Figure 138.13 illustrates this effect by comparing films #9 and #6 (sensitive to 36.8- and 15.3-MeV protons, respectively) from shot 63035. The diameter of the white ring is reduced by about 15% in film #6 with respect to that in film #9. This reduction is too significant to be explained by the variation of the image magnification factor because of the finite thickness of the film pack (this explains the less-than-1% difference) and by the difference of the evolution time between the films because of the proton time-of-flight difference. A plausible explanation of this effect is a negative charging of the target. The lower-energy protons are more susceptible to deflection by the force from the

charge and form a smaller ring, while the higher-energy protons are less susceptible and form a larger ring. The measured ring diameters can be explained if the target charge  $Q \approx -7 \times 10^{10} e$ , corresponding to an electric field  $\approx 6 \times 10^6 \text{ V/cm}$  at the critical radius. A possible mechanism of this charging is presented in **Discussion and Conclusions**, p. 118.

Features from the stalk mount and related perturbations in the target corona can be seen in the lower part of the radiographs in Fig. 138.12. The vertical features denoted by C are projections of the stalk and do not significantly vary in time. The upper end of the stalk image in Figs. 138.12(a) and 138.12(b) is located inside the white ring B associated with the critical surface. This is because of the stalk inclination with respect to the imaging axis (see Fig. 138.11), so that the stalk end is projected inside the target radius. Electromagnetic fields developed at material interfaces resulting from the interactions of plasmas ablated from the stalk, glue, and target produce variously shaped structures denoted by D. These structures evolve taking bow- and cylinder-like shapes at an earlier time [see Figs. 138.12(a) and 138.12(b)] and cone-like shapes at a later time [see Figs. 138.12(c) and 138.12(d)].

The feature F in Figs. 138.12(a), 138.12(c), and 138.12(d) is an image of the Cu wires and consists of light and dark horizontal lines crossing the target images in the midplane. These lines are formed because of focusing or defocusing protons by electromagnetic fields near the wires. The lines in Figs. 138.12(a) and 138.12(c) are produced by the wires located on the target side facing the proton detector. These lines demonstrate a complicated internal structure, showing tiny dark lines located inside wide light lines. The latter light lines end between the two other dark lines. The observed line structures suggest [and simulations confirm (see **Simulation Results**, p. 114)] that the fields deflect at least a fraction of backlighting protons toward the wire (focusing the beams) and form the interleaved dark and light lines on the detector plane. The width of the line structures increases from Fig. 138.12(a) to 138.12(c), indicating that the fields become stronger or occupy a larger area at a later time. Figure 138.12(d) shows a line structure produced by the wire located on the target side facing the proton source. An apparent dark horizontal line is located a little above the target image's midplane and a less-apparent line just below that plane. The image of the latter line is probably obscured by electromagnetic fields developed in the corona and observed as "cloudy" structures in the central part of Fig. 138.12(d). Simulations suggest (see **Simulation Results**, p. 114) that the line structure in Fig. 138.12(d) is formed by protons deflected from the wire (defocused beams).

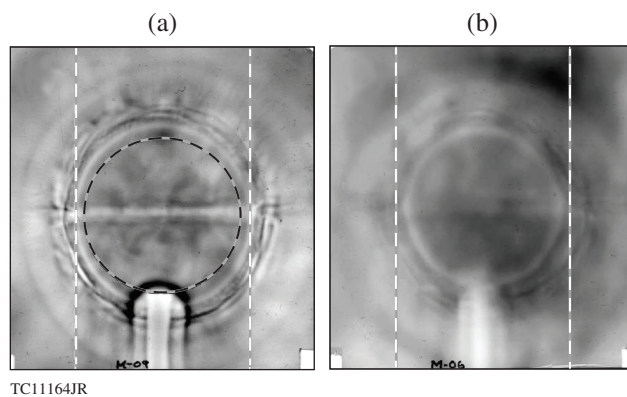


Figure 138.13  
Comparison of radiographs from films (a) #9 and (b) #6 for shot 63035. These films are primarily sensitive to 36.8- and 15.3-MeV protons, respectively. The vertical white dashed lines [in (a) and (b)] mark the diameter of the white ring in (a). The diameter of the similar ring in (b) is reduced by about 15%, indicating negative charging of the target. The dashed black circle in (a) shows the projection of the initial target surface (within  $\approx 5\%$  accuracy).

Figures 138.12(c) and 138.12(d) allow one to study almost identical plasma and field structures from the wires by probing them with protons from opposite directions. Changing the direction changes the sign of the Lorentz force acting on the protons, whereas the electric force is not changed. Therefore, the differences observed in Figs. 138.12(c) and 138.12(d) can be attributed to only the effects of magnetic fields.

Figure 138.12(b) shows the target with the glue spot on the side facing the detector at  $t = 525$  ps. This spot produces the light spot G in the center of the radiograph. The diameter of spot G is about a factor of 2 larger than the projected diameter of the glue spot of an undriven target, indicating the effects of electromagnetic fields. The geometry of deflected proton beams (convergent or divergent) and, accordingly, the sign of the corresponding self-generated magnetic fields around the spot are difficult to determine using only this measurement. Both the convergent and divergent beams can form light spots on radiographs if deflection angles are large enough. Numerical simulations suggest (see the next section) that the light spot is produced by divergent (defocused) proton beams.

### Simulation Results

The experiments were simulated using the 2-D hydrodynamic code *DRACO*.<sup>27</sup> *DRACO* solves the induction equation in the form based on the Braginskii MHD model.<sup>1</sup>

The code includes the effects of magnetic fields on the heat transport: the modified Spitzer flux, cross-gradient heat flux, and heat flux caused by electron currents.<sup>1</sup> The induction equation and field-modified heat flux are described in the **Appendix** (p. 119). The simulations assume the axial symmetry and start from a zero-field condition. Self-generated fields, therefore, develop only the azimuthal component  $\mathbf{B} = (0,0,B_\phi)$ .

Measured proton radiographs were compared with synthetic radiographs that were calculated using a proton ray-trace code. The code employs the equation of motion for protons, which includes the effect of magnetic and electric fields,

$$M_p \frac{d\mathbf{V}}{dt} = \frac{e}{c} \mathbf{V} \times \mathbf{B} - \frac{1}{n_e} (\nabla P_e - \mathbf{R}_T), \quad (1)$$

where  $M_p$  and  $\mathbf{V}$  are the proton mass and velocity, respectively,  $P_e$  is the electron pressure, and  $\mathbf{R}_T$  is the thermoelectric force (see **Appendix**, p. 119). The first and second terms on the right-hand side of Eq. (1) represent the Lorentz and electric forces, respectively. The calculations assume the same proton backlighting geometry as in the experiment (Fig. 138.10). The proton source is approximated by a monoenergetic point

source. Images are constructed by collecting all protons crossing the detector plane. The change in proton energy caused by interactions with electric fields is small and neglected. The effects of the scattering and stopping of protons caused by elastic and nonelastic collisions with background ions are small and also neglected.<sup>22</sup>

Figure 138.14 shows simulation results of the target with a stalk at  $t = 770$  ps. This time corresponds to that in Figs. 138.12(c) and 138.12(d). The density distribution in Fig. 138.14(a) shows that the stalk and target shell are compressed by shocks. The shock in the shell has already experienced a breakout, and the shell has moved about  $40 \mu\text{m}$  inward from the initial position. The flows ablated from the stalk and glue interact with the spherical outflow from the

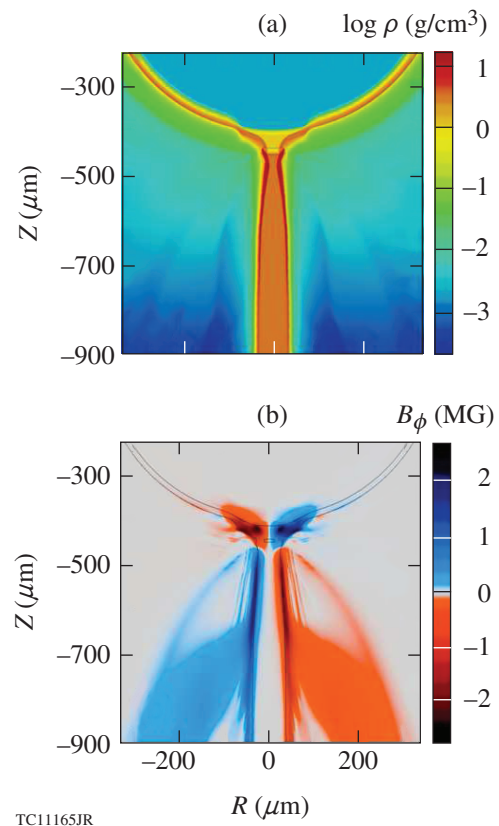


Figure 138.14

Snapshots from axisymmetric *DRACO* simulations of the target with a stalk at  $t = 770$  ps. (a) Density distribution. The region around the target and stalk joint is shown. The target center is at  $(0,0)$ . (b) Distribution of the magnetic induction  $B_\phi$ . The negative sign of  $B_\phi$  corresponds to magnetic fields directed toward the reader and the positive sign away from the reader. The black contours represent a density of  $1.2 \text{ g/cm}^3$ .

target, forming cone-like interfaces between the materials. This produces nonuniform electron density and temperature distributions, which result in the self-generated magnetic fields shown in Fig. 138.14(b). These fields grow to  $\sim 3$  MG and are mainly generated near the ablation and critical surfaces, where the source term ( $\sim \nabla T_e \times \nabla n_e$ ) takes the maximum value. The fields are concentrated near the ablation surfaces and not convected outward by the ablation flows as one can expect in the case of the ideal MHD. This concentration and the absence of the flow convection are caused by the Nernst convection, which compresses the fields toward the ablation surfaces and significantly overcomes the flow convection. The fields around the stalk produce cross-gradient heat fluxes, which are directed outward and convect (by the Nernst convection) several magnetic fields. This explains the concentration of fields around the stalk at  $Z \approx -600 \mu\text{m}$  in Fig. 138.14(b). Other magnetic fields that are localized at the material interfaces in the corona form cone-like structures. The field structure around the target with the stalk is schematically illustrated in Fig. 138.15.

Figures 138.16(a)–138.16(c) show synthetic radiographs of the implosion target with the stalk at  $t = 300, 525,$  and

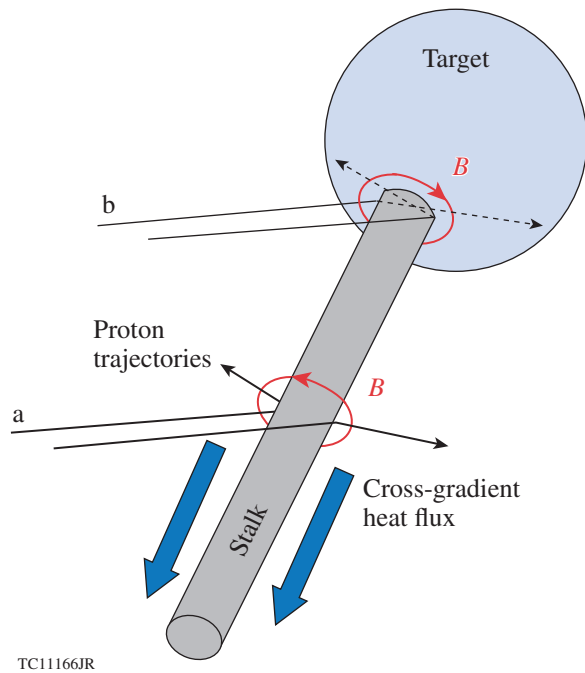


Figure 138.15

Schematic view of self-generated magnetic fields (in red) near the target and stalk joint and around the stalk. Backlighting protons (black lines) are deflected by the fields, causing trajectories “a” to diverge and “b” to converge. The fields around the stalk produce a cross-gradient heat flux, which is directed away from the target.

770 ps, respectively. The center of the target is projected in the center of the radiographs, and the stalk is inclined at the same  $42^\circ$  angle with respect to the imaging axis as in the experiment. Features C and D from the stalk are observed in the lower part of the radiographs. These features closely resemble the similar features of C and D in the measured radiographs in Fig. 138.12. An analysis of the simulations shows that the vertical feature C is formed because of protons deflected by the fields at the ablation surface around the stalk (the trajectories “a” in Fig. 138.15). The fields at the material interfaces in the corona produce the feature D. The change of the measured shapes of these features in time [compare Figs. 138.12(a)–138.12(c) and Figs. 138.16(a)–138.16(c), respectively] is well produced in the simulations.

In Fig. 138.16, features C and D result from protons deflected by magnetic fields while the effects of electric fields are not significant. As an example, the radiograph in Fig. 138.16(d) was calculated without the Lorentz force term in Eq. (1) and does not show these features. Instead, this radiograph reveals the feature H, which is not clearly seen in Fig. 138.16(c) and was developed as a result of electric fields at the standing shock in the plasma ablated from the stalk.

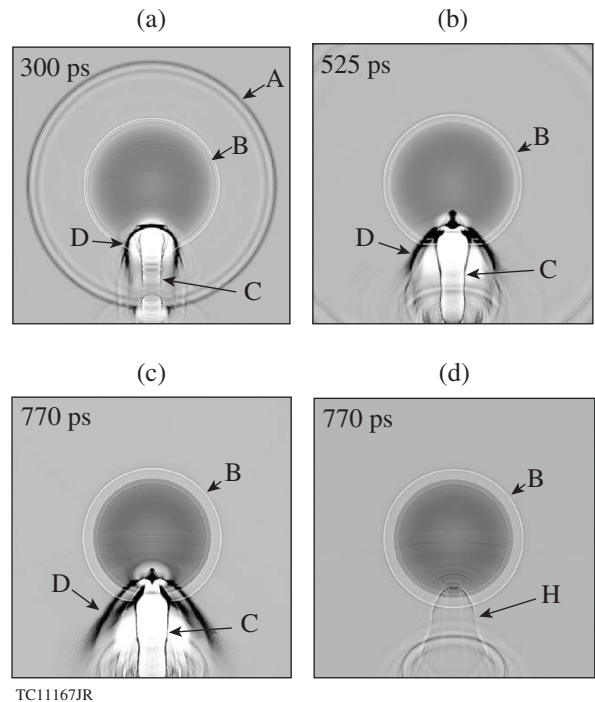


Figure 138.16

Synthetic proton radiographs of the target with a stalk at (a)  $t = 300$  ps, (b) 525 ps, and [(c) and (d)] 770 ps. Radiographs (a)–(c) were simulated using both the electric and magnetic terms in Eq. (1); radiograph (d) was simulated using only the electric term.

The radiographs in Fig. 138.16 reveal rings A and B, which are similar to those in the measured radiographs in Fig. 138.12. The simulations suggest that ring A develops because of protons deflected by electric fields at the front of the expanding plasma corona and rings B develop because of protons deflected at the critical surface. Magnetic fields are insignificant here because the corona front and critical surface are almost spherically symmetric, resulting in a small magnetic source.

Figure 138.17(a) shows the radial distribution of the electric force acting on protons in the radial direction from the *DRACO* model shown in Fig. 138.14, but at  $t = 300$  ps; Fig. 138.17(b) shows the corresponding distributions of  $P_e$ ,  $T_e$ , and  $n_e/n_{cr}$ . The plotted distributions are for the upper (not perturbed by the stalk) hemisphere. The vertical dashed lines 1, 2, and 3 show the location of the ablation, critical, and corona fronts, respectively. The electric force has a negative sign between lines 1 and 2 and a positive sign between lines 2 and 3. As a result, protons flying at the radius range between lines 1 and 2 are deflected toward the target center, whereas protons flying at the range between lines 2 and 3 are deflected outward. This causes the white ring B in Fig. 138.16(a) to appear at the critical surface along with two dark rings: one just inside the white ring in the place of the ablation surface and another, ring A, in the corona front. It should be noted that the MHD model in *DRACO* is inaccurate when the free path of charged particles is larger than the characteristic scale lengths, which follow from the model. This could happen in the corona and, in particular, at the corona's front. Nevertheless, *DRACO* simulations reproduce well the measurements of ring A (Fig. 138.12).

The density [Figs. 138.18(a) and 138.18(c)] and magnetic induction [Figs. 138.18(b) and 138.18(d)] are shown at two

consecutive times,  $t = 300$  and  $770$  ps, from simulations of the target with the Cu wire. The  $20\text{-}\mu\text{m}$ -diam wire is located near the equatorial plane. At  $t = 300$  ps, the wire has been compressed by the shock, and perturbations have been introduced at the target ablation surface and in the corona [Fig. 138.18(a)]. Self-generated magnetic fields [Fig. 138.18(b)] are localized around the wire and end somewhere between the ablation and critical surfaces because of the Nernst convection. These fields

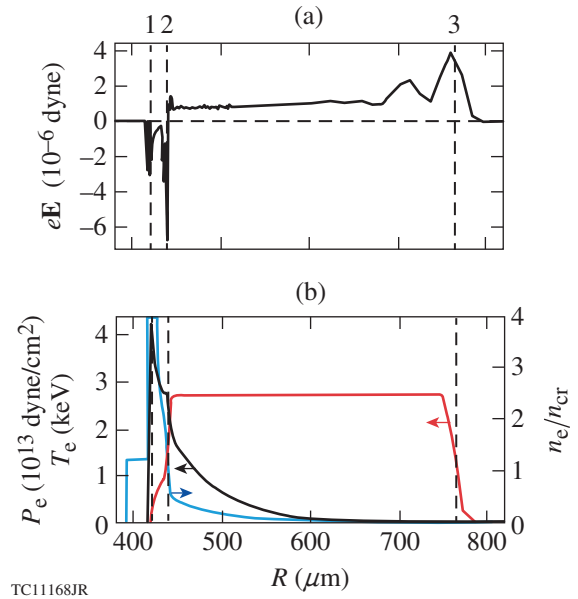


Figure 138.17 Radial profiles of selected quantities from the implosion simulation at  $t = 300$  ps. (a) Radial component of the electric force acting on protons,  $eE = -(\nabla P_e - \mathbf{R}_T)/n_e$ . The vertical dashed lines 1, 2, and 3 indicate the locations of the ablation, critical density, and outer plasma fronts, respectively. (b) Electron pressure (black), number density (blue), and temperature (red).

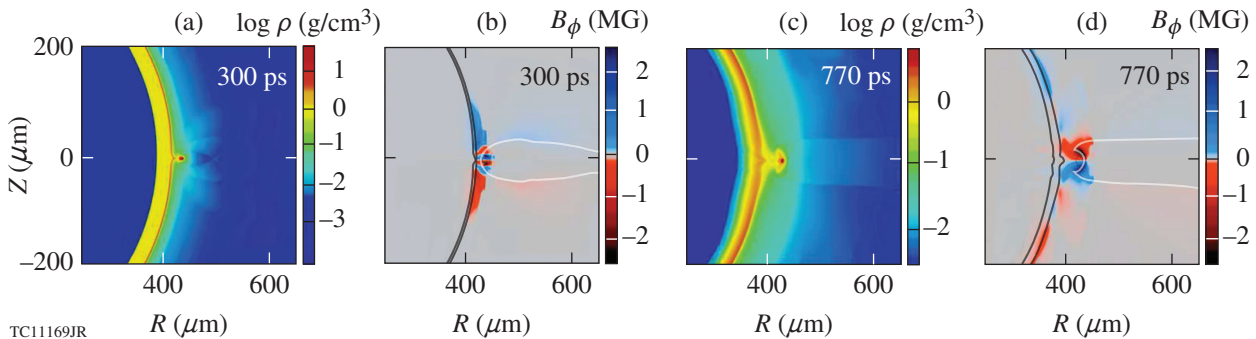


Figure 138.18 Snapshots from axisymmetric *DRACO* simulations of the target with a Cu wire. [(a) and (c)] Distributions of the density at  $t = 300$  and  $770$  ps, respectively. The wire is located near the equatorial plane. Laser light comes from the right. [(b) and (d)] Distributions of  $B_\phi$  at the same moments as (a) and (c). The black contours represent a density of  $1.2\text{ g/cm}^3$ , and the white contours show the interface between the Cu and CH plasmas in the corona.

grow to  $\sim 2$  MG and change their sign several times in the polar direction. Magnetic fields of small value also develop at the Cu and CH material interface in the corona [the interface is shown by the white line in Fig. 138.18(b)]. At the later time,  $t = 770$  ps, the remnant of the wire is located at a larger offset from the shell [Fig. 138.18(c)], and the fields, about 2 MG, are more evenly distributed around the wire and occupy the relatively large volume [Fig. 138.18(d)]. The largest fields at this time end again between the ablation and critical surfaces, which are more radially separated. As in the early time, there are small fields at the material interface in the corona. Note that the fields immediately around the wire change their sign during the evolution [compare Figs. 138.18(b) and 138.18(d)]. Figure 138.19 schematically illustrates the field topology around the wire at  $t = 770$  ps.

Synthetic radiographs in Figs. 138.20(a), 138.20(c), and 138.20(d) show the target with the wire at  $t = 300$ , 770, and 770 ps, respectively. The wire is located on the target side facing the proton detector in Figs. 138.20(a) and 138.20(c) and the source in Fig. 138.20(d). The feature F in the images is from the wire and can be compared with the analogous feature F in the measured radiographs in Fig. 138.12. At  $t = 300$  ps, the synthetic image consists of a white line that ends between two dark lines [Fig. 138.20(a)]. This white line is not uniform and includes two tiny dark lines inside of it. A similar, but not identical, line structure was observed in Fig. 138.12(a). The differences between the measured and simulated images could be attributed to the experimental blurring, which can wash out fine structures and was not considered in the ray-trace code. The synthetic image of the wire at  $t = 770$  ps in Fig. 138.20(c) reproduces the thin dark line in the middle of the wide light line similar to the one measured [see Fig. 138.12(c)]. This dark line, however, is much clearer in the synthetic image. An analysis of the simulations shows that the white and black lines in Figs. 138.20(a) and 138.20(c) are formed by deflect-

ing (focusing) the protons (which traverse the regions with the fields immediately adjacent to the wire) toward the wire [Fig. 138.19(b)]. When the target is probed by protons from the opposite direction, the proton trajectories are defocused by the fields [Fig. 138.19(a)] forming the two dark lines F in Fig. 138.20(d). The corresponding measured radiograph in Fig. 138.12(d) shows the clear image of only one (upper) dark line, while the other (lower) dark line is represented unclearly, probably because of scattering backlighting protons by electromagnetic fields in the corona.

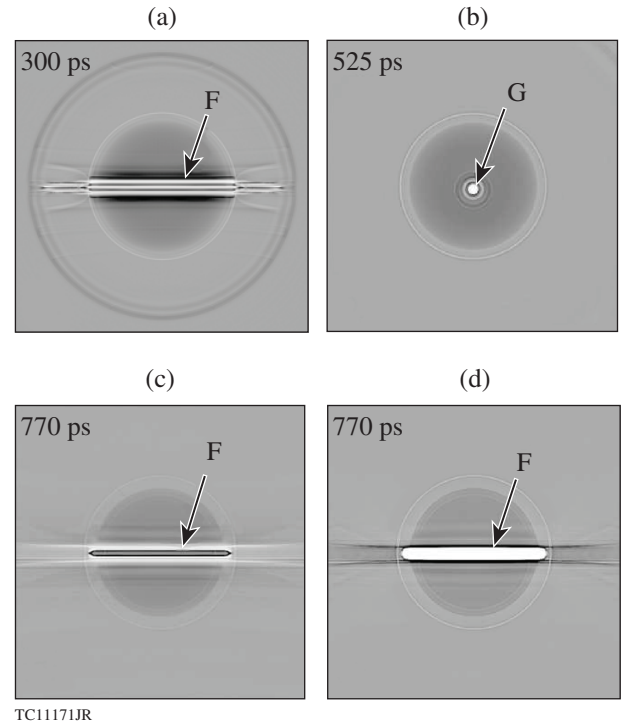


Figure 138.20 Synthetic proton radiographs of the targets with a wire [(a), (c), and (d)] and a glue spot (b). The backlighting geometry corresponds to that for the measured radiographs in Fig. 138.12.

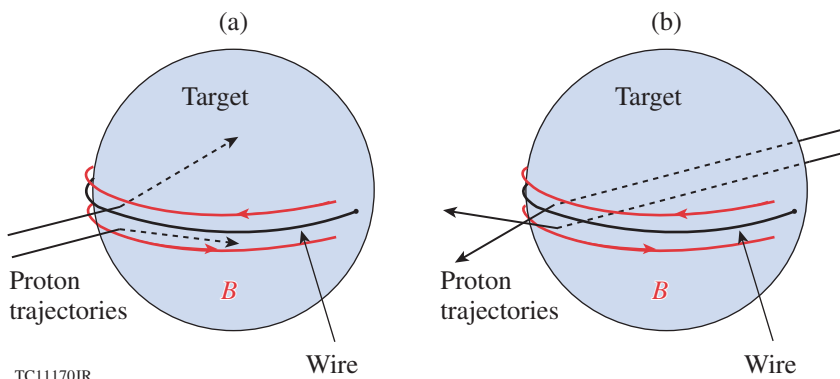


Figure 138.19 Schematic view of self-generated magnetic fields (in red) near the wire. (a) Backlighting protons come from the left (black lines), illustrating the experimental conditions when the wire is located on the target side facing the proton source. The proton trajectories are deflected by the fields and diverge. (b) The proton trajectories coming from the opposite direction (the wire on the side facing the proton detector) converge.

Figure 138.21 shows simulation results of the target with a 50- $\mu\text{m}$ -diam glue spot at  $t = 525$  ps. Perturbations introduced by the spot [Fig. 138.21(a)] result in self-generated fields up to  $\sim 4$  MG that are localized at the ablation surface around the spot [Fig. 138.21(b)]. As mentioned earlier, this localization is caused by the Nernst convection. It is worth noting that the field around the spot has the opposite sign to that of the wire in Fig. 138.18(d) and the same sign as the field near the target and stalk joint in Fig. 138.14(b). Figure 138.22 illustrates the topology of the fields around the glue spot.

Figure 138.20(b) shows a synthetic radiograph of the target with the glue spot. The radiograph was calculated assuming the same spot location as in the experiment (facing the detector). The image G of the spot consists of a white circle surrounded by a sequence of fine dark and white rings. The measured radiograph confirms the development of the white

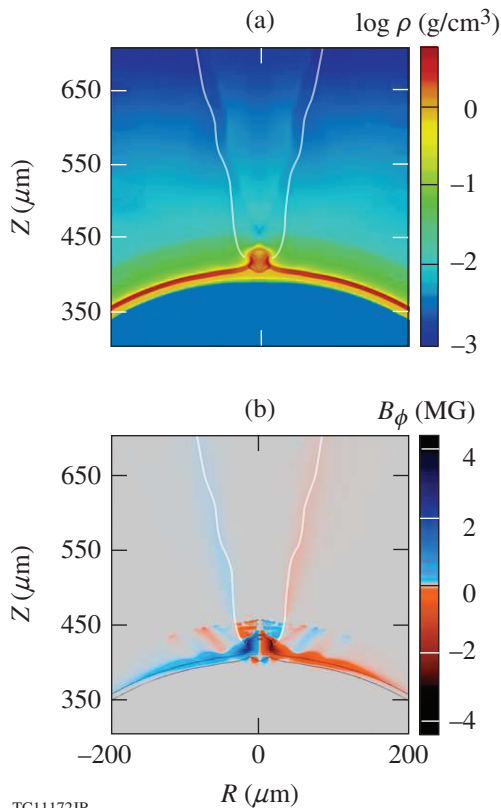


Figure 138.21 Snapshots from axisymmetric *DRACO* simulations of the target with the glue spot at  $t = 525$  ps. Distributions of the (a) density and (b)  $B_\phi$ . The glue spot is located at the pole. Laser light comes from the top. The black contours in (b) represent a density of 1.2 g/cm<sup>3</sup> and the white contours in (a) and (b) show the interface between the glue and CH plasmas in the corona.

circle showing the light spot in the center of Fig. 138.12(b); however, there is no signature of the ring structures around the spot. The lack of these structures could be a result of either an inaccuracy in modeling or experimental blurring. The origin of the white circle is illustrated in Fig. 138.22, which shows that protons traversing the region near the glue spot are deflected off (defocused), producing a circle of reduced proton fluence on the detector plane.

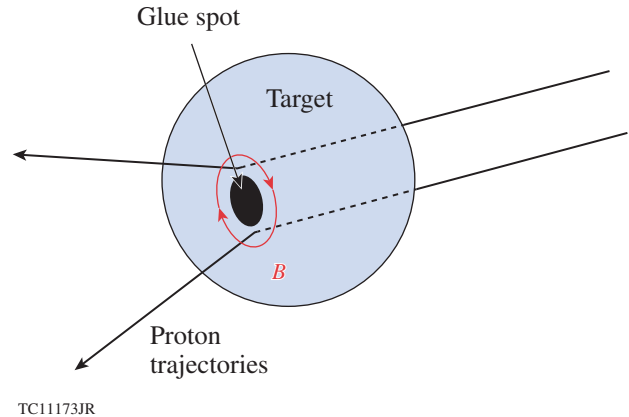


Figure 138.22 Schematic view of self-generated magnetic fields (in red) around the glue spot. The experimental conditions (the spot on the target side facing the proton detector) are illustrated by showing protons coming from the right (black lines). These protons diverge after interacting with the fields.

### Discussion and Conclusions

Electric and self-generated magnetic fields have been measured in implosion experiments on the OMEGA laser using plastic-shell targets. The self-generated fields developed as a result of perturbations from the mount stalk and imposing surface defects: Cu wires and glue spots (Fig. 138.11). The electric and magnetic fields were measured using the TNSA radiography, in which a proton beam was produced by employing a high-intensity OMEGA EP laser beam. Good-quality radiographs were obtained using 37-MeV backlighting protons. These radiographs show clear features from the stalk, wire, and glue spot in different times and different backlighting geometries (Fig. 138.12).

Synthetic proton radiographs (Figs. 138.16 and 138.20) were calculated by post-processing 2-D MHD *DRACO* simulations and, when compared with the measured radiographs, demonstrated good agreement. The inclusion of the  $\nabla T_e \times \nabla n_e$  source, Nernst convection, and anisotropic resistivity in the induction equation and the field-modified heat fluxes in the electron energy equation is essential to obtaining this agreement. The ring-like features in the measured and synthetic radiographs

(Figs. 138.12, 138.16, and 138.20) are explained by protons deflected by electric fields up to  $\sim 10^7$  V/cm at the critical surface (white rings) and the plasma corona front (outer dark rings). The features from the defects (stalks, wires, and glue spots) are developed mostly by protons deflected by magnetic fields up to  $\sim 3$  MG. This was demonstrated by calculating the radiographs with and without magnetic fields (but with electric fields in both cases). The features from the defects disappeared in the calculations without magnetic fields, while the ring-like features were not changed with or without the fields.

The white rings in the radiographs in Figs. 138.12 and 138.13 are explained by scattering protons off at the critical radius by electric fields (Fig. 138.17). An alternative explanation of such rings could be that protons are scattered through Coulomb collisions with ions in the dense shell.<sup>25</sup> The TNSA radiography of undriven targets using the lowest-energy protons indeed demonstrated this possibility.<sup>15</sup> Coulomb collisions are unlikely responsible, however, for the observation of the rings in the present experiment for at least two reasons: (1) Trajectories of 37-MeV protons used in the experiment are not significantly affected by Coulomb collisions.<sup>22</sup> (2) The measured radius of the white rings is larger than the target radius (see the dashed black circle in Fig. 138.13) and consistent with numerical estimates of the critical radius.

Proton radiographs reveal a reduction in the white-ring radii, which are associated with the target's critical surface, for the lower-energy protons (Fig. 138.13). This reduction can be explained by the negative charging of the target within the critical surface with the charge  $Q \approx -7 \times 10^{10} e$ . Electrostatic charging of targets has been studied using fusion-based proton radiography<sup>25</sup> and measuring energetic ( $\geq 1$ -MeV) fast protons and ions<sup>34,35</sup> in direct-drive implosions. This charging is likely provided by hot electrons ( $\sim 10$  to 100 keV) generated by the two-plasmon-decay (TPD) instability developed near the radius of the quarter-critical density.<sup>36</sup> The charging observed in the present experiment probably comes from the same source: a fraction of the hot TPD electrons moves inward and creates an electrostatic potential difference between the quarter-critical-density region (positively charged) and the target shell (negatively charged). The energy needed to produce the inferred charge is a very small fraction of the incident laser energy  $E \sim Q^2/R_t \sim 2 \times 10^{-3}$  J. The energy to support this charging during the implosion, however, could be significantly larger because of dissipations in the associated return currents.

Electromagnetic fields around mount stalks supporting laser-irradiated targets have been measured using monoener-

getic ( $\sim 3.3$ -MeV) proton radiography.<sup>37</sup> A source of the fields in this experiment was believed to be a return current of up to  $\sim 7$  kA driven through the stalk from positively charged targets. This current created toroidal magnetic fields of  $\sim 10^4$  G. Considering the inferred magnitude of magnetic fields from the return currents versus the magnitude of self-generated fields around the stalk in the present experiment [ $\sim$ MG (see Fig. 138.14)], one concludes that it is unlikely these currents make a significant contribution to image C of the stalks in Fig. 138.12.

The measured radiographs show ripple structures quasi-spherically distributed around the targets (feature E in Fig. 138.12). These structures were not reproduced in simulations and apparently were caused by small-scale electromagnetic fields in the corona. The nature of these fields is unclear. Numerical models suggest that the ripples are localized near the radius of the quarter-critical density. It is known that various laser-plasma instabilities can develop near this radius, including stimulated Brillouin and Raman scatterings and TPD instability.<sup>36</sup> It is plausible that the observed ripples are related to electromagnetic fields caused by these instabilities.

The simulations have demonstrated the effect of self-generated magnetic fields on the dynamics of laser-ablated plasma. This effect occurs as a result of changing heat fluxes by the fields in the conduction zone, when  $\omega_e \tau_e \geq 0.3$ . In this case, the fluxes are suppressed in one direction and, being redirected, amplified in another direction. Such a redirection of the fluxes causes the change in the ablation pressure near the perturbations, which, in turn, causes the change in the perturbations. The dynamic effect of the field-modified heat fluxes, however, was found to be not significant enough to be observed in the present experiment.

#### ACKNOWLEDGMENT

This material is based upon work supported by the Department of Energy National Nuclear Security Administration under Award Number DE-NA0001944, the University of Rochester, and the New York State Energy Research and Development Authority. The support of DOE does not constitute an endorsement by DOE of the views expressed in this article.

#### Appendix: MHD Numerical Method

Electric and self-generated magnetic fields in implosion targets are simulated by employing the 2-D hydrodynamic ICF code *DRACO*,<sup>27</sup> which uses the Eulerian hydrodynamics and has been modified to solve the induction equation and include the effects of magnetic fields on the heat transport and plasma dynamics. The flow is assumed to be axisymmetric and the magnetic field has only the azimuthal component  $\mathbf{B} = (0, 0, B_\phi)$ . The induction equation is used in the Braginskii's form<sup>1</sup>

$$\frac{\partial \mathbf{B}}{\partial t} = \nabla \times (\mathbf{V} \times \mathbf{B}) + \frac{c}{e} \nabla \times \frac{\nabla P_e}{n_e} - \nabla \times \frac{\mathbf{j} \times \mathbf{B}}{en_e} - \frac{c}{e} \nabla \times \frac{\mathbf{R}}{n_e}, \quad (\text{A1})$$

where  $\mathbf{V} = V_r, V_\theta, 0$  is the flow velocity and  $\mathbf{j} = (c/4\pi)\nabla \times \mathbf{B}$  is the current density. The force  $\mathbf{R}$  acts on electrons and consists of two components:  $\mathbf{R} = \mathbf{R}_u + \mathbf{R}_T$ , where

$$\mathbf{R}_u = -\alpha_\perp u_\perp + \alpha_\Lambda (\mathbf{h} \times \mathbf{u}) \quad (\text{A2})$$

is the friction force and

$$\mathbf{R}_T = -\beta_\perp^{uT} \nabla_\perp T_e - \beta_\perp^{uT} (\mathbf{h} \times \nabla T_e) \quad (\text{A3})$$

is the thermal force,  $\mathbf{u} = -\mathbf{j}/en_e$  is the electron-ion relative velocity, and  $\mathbf{h}$  is the unit vector in the  $\phi$  direction. The subscript “ $\perp$ ” in Eqs. (A3) and (A4) refers to vector components tangential to  $\mathbf{B}$ .

The electron heat flux is represented by two components:  $\mathbf{q}_e = \mathbf{q}_T^e + \mathbf{q}_u^e$ , where

$$\mathbf{q}_T^e = -\kappa_\perp^e \nabla_\perp T_e - \kappa_\Lambda^e (\mathbf{h} \times \nabla T_e) \quad (\text{A4})$$

is the thermal component, which consists of the modified Spitzer flux<sup>8</sup> and lateral (cross-gradient) flux (the first and second terms on the right-hand side, respectively), and

$$\mathbf{q}_u^e = -\beta_\perp^{Tu} u_\perp + \beta_\Lambda^{Tu} (\mathbf{h} \times \mathbf{u}) \quad (\text{A5})$$

is the friction component. The coefficients  $\beta_\perp^{uT}, \beta_\Lambda^{uT}, \beta_\perp^{Tu}, \beta_\Lambda^{Tu}, \alpha_\perp, \alpha_\Lambda, \kappa_\perp^e$ , and  $\kappa_\Lambda^e$  in Eqs. (A3)–(A6) are defined in Ref. 1 as functions of the Hall parameter  $\omega_e \tau_e$  and the ion charge  $Z$ . The standard flux limitation<sup>38</sup> (with the flux-limiter parameter  $f = 0.06$ ) of the thermal component  $\mathbf{q}_T^e$  is applied to mimic energy losses because of cross-beam energy transfer.<sup>39</sup>

The release of energy caused by magnetic dissipation is accounted for by adding the term

$$Q_e = -\mathbf{R} \cdot \mathbf{u} \quad (\text{A6})$$

in the energy equation for electrons. The dynamic effects of magnetic fields are described by the magnetic force term

$$\mathbf{F}_m = \frac{1}{c} (\mathbf{j} \times \mathbf{B}) \quad (\text{A7})$$

in the equation of motion.

The MHD approximation fails when the free path of charged particles exceeds the characteristic scale lengths of a problem. In implosion simulations, such conditions, for example, can appear at the front of plasma, expanding into vacuum. A simple application of Eq. (A1) in these conditions can result in a significant overestimation of self-generated magnetic fields. To prevent such an unphysical behavior, calculations of spatial derivatives in the source and pinch terms of Eq. (A1) (the second and fourth, and third terms, respectively, on the right-hand side of this equation) should use limited scale lengths: they cannot be smaller than the electron free path  $\ell_e$ . In practice, the limitation is implemented by substituting the grid size  $\Delta x$  by  $\max(\Delta x, \epsilon \ell_e)$  when calculating the derivative  $\partial f / \partial x \approx \Delta f / \Delta x$ . Here,  $\epsilon$  is a parameter of an order of unity.

## REFERENCES

1. S. I. Braginskii, in *Reviews of Plasma Physics*, edited by Acad. M. A. Leontovich (Consultants Bureau, New York, 1965), Vol. 1, p. 205.
2. V. V. Korobkin and R. V. Serov, *JETP Lett.* **4**, 70 (1966).
3. G. A. Askar'yan *et al.*, *JETP Lett.* **5**, 93 (1967).
4. J. A. Stamper *et al.*, *Phys. Rev. Lett.* **26**, 1012 (1971).
5. A. Raven, O. Willi, and P. T. Rumsby, *Phys. Rev. Lett.* **41**, 554 (1978).
6. S. Atzeni and J. Meyer-ter-Vehn, *The Physics of Inertial Fusion: Beam Plasma Interaction, Hydrodynamics, Hot Dense Matter*, International Series of Monographs on Physics (Clarendon Press, Oxford, 2004), pp. 47–50.
7. B. H. Ripin *et al.*, *Phys. Rev. Lett.* **34**, 1313 (1975).
8. L. Spitzer, Jr. and R. Härm, *Phys. Rev.* **89**, 977 (1953).
9. A. Nishiguchi, *Jpn. J. Appl. Phys.* **41**, 326 (2002).
10. T. R. Boehly, D. L. Brown, R. S. Craxton, R. L. Keck, J. P. Knauer, J. H. Kelly, T. J. Kessler, S. A. Kumpan, S. J. Loucks, S. A. Letzring, F. J. Marshall, R. L. McCrory, S. F. B. Morse, W. Seka, J. M. Soares, and C. P. Verdon, *Opt. Commun.* **133**, 495 (1997).
11. M. Tatarakis *et al.*, *Nature* **415**, 280 (2002).
12. M. Borghesi *et al.*, *Laser Part. Beams* **20**, 269 (2002).
13. C. K. Li, F. H. Séguin, J. A. Frenje, J. R. Rygg, R. D. Petrasso, R. P. J. Town, P. A. Amendt, S. P. Hatchett, O. L. Landen, A. J. Mackinnon, P. K. Patel, V. Smalyuk, J. P. Knauer, T. C. Sangster, and C. Stoeckl, *Rev. Sci. Instrum.* **77**, 10E725 (2006).
14. E. L. Clark *et al.*, *Phys. Rev. Lett.* **84**, 670 (2000).
15. A. Zylstra, C. K. Li, H. G. Rinderknecht, F. H. Séguin, R. D. Petrasso, C. Stoeckl, D. D. Meyerhofer, P. Nilson, T. C. Sangster, S. Le Pape, A. Mackinnon, and P. Patel, *Rev. Sci. Instrum.* **83**, 013511 (2012).

16. A. J. Mackinnon, P. K. Patel, R. P. Town, M. J. Edwards, T. Phillips, S. C. Lerner, D. W. Price, D. Hicks, M. H. Key, S. Hatchett, S. C. Wilks, M. Borghesi, L. Romagnani, S. Kar, T. Toncian, G. Pretzler, O. Willi, M. Koenig, E. Martinolli, S. Lepape, A. Benuzzi-Mounaix, P. Audebert, J. C. Gauthier, J. King, R. Snavely, R. R. Freeman, and T. Boehly, *Rev. Sci. Instrum.* **75**, 3531 (2004).
17. J. R. Rygg, F. H. Séguin, C. K. Li, J. A. Frenje, M. J.-E. Manuel, R. D. Petrasso, R. Betti, J. A. Delettrez, O. V. Gotchev, J. P. Knauer, D. D. Meyerhofer, F. J. Marshall, C. Stoeckl, and W. Theobald, *Science* **319**, 1223 (2008).
18. C. K. Li, F. H. Séguin, J. A. Frenje, M. Manuel, D. Casey, N. Sinenian, R. D. Petrasso, P. A. Amendt, O. L. Landen, J. R. Rygg, R. P. J. Town, R. Betti, J. Delettrez, J. P. Knauer, F. Marshall, D. D. Meyerhofer, T. C. Sangster, D. Shvarts, V. A. Smalyuk, J. M. Soures, C. A. Back, J. D. Kilkenny, and A. Nikroo, *Phys. Plasmas* **16**, 056304 (2009).
19. C. K. Li, F. H. Séguin, J. A. Frenje, J. R. Rygg, R. D. Petrasso, R. P. J. Town, P. A. Amendt, S. P. Hatchett, O. L. Landen, A. J. Mackinnon, P. K. Patel, V. A. Smalyuk, T. C. Sangster, and J. P. Knauer, *Phys. Rev. Lett.* **97**, 135003 (2006).
20. P. Nicolai *et al.*, *Phys. Plasmas* **7**, 4250 (2000).
21. M. J.-E. Manuel, C. K. Li, F. H. Séguin, J. Frenje, D. T. Casey, R. D. Petrasso, S. X. Hu, R. Betti, J. D. Hager, D. D. Meyerhofer, and V. A. Smalyuk, *Phys. Rev. Lett.* **108**, 255006 (2012); M. J.-E. Manuel, C. K. Li, F. H. Séguin, J. A. Frenje, D. T. Casey, R. D. Petrasso, S. X. Hu, R. Betti, J. D. Hager, D. D. Meyerhofer, and V. Smalyuk, *Phys. Plasmas* **19**, 082710 (2012).
22. L. Gao, P. M. Nilson, I. V. Igumenshchev, S. X. Hu, J. R. Davies, C. Stoeckl, M. G. Haines, D. H. Froula, R. Betti, and D. D. Meyerhofer, *Phys. Rev. Lett.* **109**, 115001 (2012).
23. L. Gao, P. M. Nilson, I. V. Igumenshchev, G. Fiksel, R. Yan, J. R. Davies, D. Martinez, V. Smalyuk, M. G. Haines, E. G. Blackman, D. H. Froula, R. Betti, and D. D. Meyerhofer, *Phys. Rev. Lett.* **110**, 185003 (2013).
24. A. J. Mackinnon *et al.*, *Phys. Rev. Lett.* **97**, 045001 (2006).
25. F. H. Séguin, C. K. Li, M. J.-E. Manuel, H. G. Rinderknecht, N. Sinenian, J. A. Frenje, J. R. Rygg, D. G. Hicks, R. D. Petrasso, J. Delettrez, R. Betti, F. J. Marshall, and V. A. Smalyuk, *Phys. Plasmas* **19**, 012701 (2012).
26. C. K. Li, F. H. Séguin, J. R. Rygg, J. A. Frenje, M. Manuel, R. D. Petrasso, R. Betti, J. Delettrez, J. P. Knauer, F. Marshall, D. D. Meyerhofer, D. Shvarts, V. A. Smalyuk, C. Stoeckl, O. L. Landen, R. P. J. Town, C. A. Back, and J. D. Kilkenny, *Phys. Rev. Lett.* **100**, 225001 (2008).
27. D. Keller, T. J. B. Collins, J. A. Delettrez, P. W. McKenty, P. B. Radha, B. Whitney, and G. A. Moses, *Bull. Am. Phys. Soc.* **44**, 37 (1999); I. V. Igumenshchev, F. J. Marshall, J. A. Marozas, V. A. Smalyuk, R. Epstein, V. N. Goncharov, T. J. B. Collins, T. C. Sangster, and S. Skupsky, *Phys. Plasmas* **16**, 082701 (2009).
28. A. Z. Dolginov and V. A. Urpin, *Sov. Phys.-JETP* **50**, 912 (1979).
29. A. Nishiguchi *et al.*, *Phys. Rev. Lett.* **53**, 262 (1984).
30. Y. Lin, T. J. Kessler, and G. N. Lawrence, *Opt. Lett.* **20**, 764 (1995).
31. T. R. Boehly, V. A. Smalyuk, D. D. Meyerhofer, J. P. Knauer, D. K. Bradley, R. S. Craxton, M. J. Guardalben, S. Skupsky, and T. J. Kessler, *J. Appl. Phys.* **85**, 3444 (1999).
32. S. Skupsky and R. S. Craxton, *Phys. Plasmas* **6**, 2157 (1999).
33. L. J. Waxer, D. N. Maywar, J. H. Kelly, T. J. Kessler, B. E. Kruschwitz, S. J. Loucks, R. L. McCrory, D. D. Meyerhofer, S. F. B. Morse, C. Stoeckl, and J. D. Zuegel, *Opt. Photonics News* **16**, 30 (2005).
34. D. G. Hicks, C. K. Li, F. H. Séguin, J. D. Schnittman, A. K. Ram, J. A. Frenje, R. D. Petrasso, J. M. Soures, D. D. Meyerhofer, S. Roberts, C. Sorce, C. Stoeckl, T. C. Sangster, and T. W. Phillips, *Phys. Plasmas* **8**, 606 (2001).
35. N. Sinenian, A. B. Zylstra, M. J. E. Manuel, H. G. Rinderknecht, J. A. Frenje, F. H. Séguin, C. K. Li, R. D. Petrasso, V. Goncharov, J. Delettrez, I. V. Igumenshchev, D. H. Froula, C. Stoeckl, T. C. Sangster, D. D. Meyerhofer, J. A. Cobble, and D. G. Hicks, *Appl. Phys. Lett.* **101**, 114102 (2012).
36. W. L. Kruer, in *The Physics of Laser Plasma Interactions*, *Frontiers in Physics*, Vol. 73, edited by D. Pines (Addison-Wesley, Redwood City, CA, 1988).
37. M. J.-E. Manuel *et al.*, *Appl. Phys. Lett.* **100**, 203505 (2012).
38. R. C. Malone, R. L. McCrory, and R. L. Morse, *Phys. Rev. Lett.* **34**, 721 (1975).
39. I. V. Igumenshchev, D. H. Edgell, V. N. Goncharov, J. A. Delettrez, A. V. Maximov, J. F. Myatt, W. Seka, A. Shvydky, S. Skupsky, and C. Stoeckl, *Phys. Plasmas* **17**, 122708 (2010).